



## 14 GHz Schottky Diodes using a p -Doped Organic Polymer

Item Type	Article
Authors	Loganathan, Kalaivanan; Scaccabarozi, Alberto D.; Faber, Hendrik; Ferrari, Federico; Bizak, Zhanibek; Yengel, Emre; Naphade, Dipti; Gedda, Murali; He, Qiao; Solomeshch, Olga; Adilbekova, Begimai; Yarali, Emre; Tsetseris, Leonidas; Salama, Khaled N.; Heeney, Martin; Tessler, Nir; Anthopoulos, Thomas D.
Citation	Loganathan, K., Scaccabarozi, A. D., Faber, H., Ferrari, F., Bizak, Z., Yengel, E., ... Anthopoulos, T. D. (2022). 14 GHz Schottky Diodes using a p -Doped Organic Polymer. Advanced Materials, 2108524. doi:10.1002/adma.202108524
Eprint version	Post-print
DOI	<a href="https://doi.org/10.1002/adma.202108524">10.1002/adma.202108524</a>
Publisher	Wiley
Journal	Advanced Materials
Rights	Archived with thanks to Advanced Materials
Download date	21/09/2023 19:27:32
Link to Item	<a href="http://hdl.handle.net/10754/675019">http://hdl.handle.net/10754/675019</a>

## 14 GHz Schottky Diodes using a *p*-Doped Organic Polymer

Kalaivanan Loganathan<sup>□</sup>, Alberto D. Scaccabarozzi<sup>□</sup>, Hendrik Faber, Federico Ferrari, Zhanibek Bizak, Emre Yengel, Dipti R. Naphade, Murali Gedda, Qiao He, Olga Solomeshch, Begimai Adilbekova, Emre Yarali, Leonidas Tsetseris, Khaled N. Salama, Martin Heeney, Nir Tessler, and Thomas D. Anthopoulos\*

Mr. K. Loganathan, Dr. A.D. Scaccabarozzi, Dr. H. Faber, Mr. F. Ferrari, Dr. E. Yengel, Dr. D. R. Naphade, Dr. M. Gedda, Ms. B. Adilbekova, Mr. E. Yarali, and Prof. T. D. Anthopoulos

King Abdullah University of Science and Technology (KAUST),

KAUST Solar Center (KSC),

Thuwal 23955-6900,

Saudi Arabia.

<sup>□</sup> *These authors contributed equally.*

\* Correspondence author e-mail: [thomas.anthopoulos@kaust.edu.sa](mailto:thomas.anthopoulos@kaust.edu.sa);

Mr. Z. Bizak and Prof. Khaled N. Salama

King Abdullah University of Science and Technology (KAUST),

Computer, Electrical and Mathematical Sciences and Engineering (CEMSE),

Advanced Membranes and Porous Materials Center (AMPM),

Thuwal 23955-6900,

Saudi Arabia.

Dr. Q. He and Prof. M. Heeney

Department of Chemistry and Centre for Processable Electronics,

Imperial College London,

London W12 0BZ,

United Kingdom.

This article has been accepted for publication and undergone full peer review but has not been through the copyediting, typesetting, pagination and proofreading process, which may lead to differences between this version and the [Version of Record](#). Please cite this article as [doi: 10.1002/adma.202108524](https://doi.org/10.1002/adma.202108524).

This article is protected by copyright. All rights reserved.

Dr. O. Solomeshch and Prof. N. Tessler

The Zisapel Nano-Electronic Center,

Department of Electrical Engineering,

Technion-Israel Institute of Technology,

Haifa 3200, Israel.

Prof. L. Tsetseris

Department of Physics, National Technical University of Athens, GR-15780 Athens,

Greece

**Keywords:** Organic semiconductor; printed electronics, radio frequency electronics; Schottky diodes; rectifier circuits

#### Abstract

The low carrier mobility of organic semiconductors and the high parasitic resistance and capacitance often encountered in conventional organic Schottky diodes, hinder their deployment in emerging radio frequency (RF) electronics. Here we overcome these limitations by combining self-aligned asymmetric nanogap electrodes ( $\sim 25$  nm) produced by adhesion-lithography, with a high mobility organic semiconductor and demonstrate RF Schottky diodes able to operate in the 5G frequency spectrum. We used C<sub>16</sub>IDT-BT, as the high hole mobility polymer, and studied the impact of *p*-doping on the diode performance. Pristine C<sub>16</sub>IDT-BT-based diodes exhibit maximum intrinsic and extrinsic cutoff frequencies ( $f_c$ ) of  $>100$  and 6 GHz, respectively. This extraordinary performance is attributed primarily to the planar nature of the nanogap channel and the diode's small junction capacitance ( $< 2$  pF). Doping of C<sub>16</sub>IDT-BT with the molecular *p*-dopant C<sub>60</sub>F<sub>48</sub>, improves the diode's performance further by reducing the series resistance resulting to intrinsic and extrinsic  $f_c$  of  $>100$  and  $\sim 14$  GHz respectively, while the DC output voltage of a RF rectifier circuit increases by a tenfold. Our work highlights the importance of the planar nanogap architecture and paves the way for the use of organic Schottky diodes in large-area radio frequency electronics of the future.

This article is protected by copyright. All rights reserved.

**Main text**

The continuing commercial success of the internet-of-things (IoT) device ecosystem requires implementation of emerging mobile communication technologies, such as 5G & 6G, and the development of means to reliably produce and power billions of devices.<sup>[1, 2]</sup> For instance, inexpensive mass manufacturing strategies are key for the massive deployment of IoT sensor nodes, while radio frequency (RF) wireless energy harvesters (RF-WEH) is considered one of the most viable solutions for powering these distributed devices.<sup>[3]</sup> The central component that determines the frequency of operation and the power conversion efficiency of RF-WEH systems is the rectifier unit.<sup>[4]</sup> State-of-the-art rectifiers are based on Schottky diodes made from Si-CMOS and III-V semiconductor technologies.<sup>[5]</sup> Unfortunately, these technologies are characterised by limited mechanical compliance and rely on costly processing methods. An alternative option is to use organic semiconductors that are simple to process on wide range of substrate materials using up-scalable printing techniques.<sup>[6]</sup> Unfortunately, to date the deployment of organic semiconductors in rectifier circuits is hindered by their relatively low operating frequency ( $f_c$ ) given by:<sup>[1, 7]</sup>

$$f_c = \frac{1}{2\pi R_s C_j} \quad (1)$$

where,  $R_s$  is the series resistance and  $C_j$  the junction capacitance of the diode. For conventional sandwich organic diode architectures these parameters are always relatively high, ultimately limiting the frequency response of the device. In order to overcome these limitations, the development of advanced diode architectures and improved material formulations with enhanced charge mobility, is urgently required.

Here, we used adhesion lithography (a-Lith)<sup>[8]</sup> to fabricate self-aligned, asymmetric (Al, Au) planar metal electrodes separated by a  $\leq 25$  nm nanogap. The advantageous co-planar electrode

architecture yields devices with low capacitance ( $< \text{pF}$ ), which is a prerequisite for high frequency operation.<sup>[9]</sup> To test this hypothesis we combined the self-aligned nanogap electrodes with a high mobility poly(indacenodithiophene-co-benzothiadiazole) ( $\text{C}_{16}\text{IDT-BT}$ ) organic semiconductor to produce planar  $p$ -type Schottky diodes, where Au and Al provide the Ohmic and rectifying contacts, respectively. The ensuing diodes were found to exhibit exceptionally high intrinsic and extrinsic frequencies of  $>100$  GHz and 6 GHz, outperforming all previously reported organic diodes. We also investigated the impact of  $p$ -doping the  $\text{C}_{16}\text{IDT-BT}$  with  $\text{C}_{60}\text{F}_{48}$ , and showed that optimal doping results to a record extrinsic cut-off frequency of  $\sim 14$  GHz and to a tenfold improvement of the direct current (DC) output voltage of rectifier circuits.

**Figure 1a** depicts the a-Lith steps used to manufacture the self-aligned asymmetric electrode nanogaps on wafer scale, while **Figure S1** presents photographs of the actual wafer at each processing step (*Supporting Information*). Further details of the a-Lith process can be found in the *Experimental* section and in our previous publications.<sup>[10-12]</sup> In brief, a-Lith relies on the application of a self-assembled monolayer (SAM), in this case octadecyl phosphonic acid (ODPA), onto the surface of the lightly oxidized first metal electrode (M1, i.e. Al). The metallophilic SAM makes the surface of M1 highly hydrophobic which in turn reduces the adhesion with the subsequently deposited second metal electrode (M2), while leaving the substrate's surface unchanged. A peel-off step is then applied to remove (i.e. mechanically delaminate) regions of M2 (Au) overlapping with M1 (Al-SAM) (**Figure 1a**). The remaining SAM present on the surface of M1 can then be removed by exposing the wafer to Ar plasma for a few seconds. The ensuing structures are self-aligned a/symmetric M1-M2 nanogaps of arbitrary shape and size. **Figure 1b** shows a photograph of a 4-inch wafer containing a large number of circular Al-Au nanogap arrays (inset), with the overlapping M1-M2 regions just being removed (mechanically peeled-off) using glue. In these planar diodes, the width ( $W$ ) of the nanogap is defined by the circumference of the inner Au electrode and for this particular experiment was varied from 250 to 5000  $\mu\text{m}$ . **Figure 1c** shows an isolated co-planar Al-Au nanogap device with

$W = 500\ \mu\text{m}$ , while **Figure 1d** displays an SEM image of the nanogap. Estimation of the inter-electrode distance (i.e. nanogap) was performed using the method derived from Kano *et al.*,<sup>[13]</sup> and used recently by our group.<sup>[10]</sup> **Figure 1e** shows the distribution of the nanogap size extracted from SEM images of five different samples from three different production batches (see **Figure S2**). The majority peak is centred on a nanogap size of 22.9 nm with a secondary peak at higher values. Variations in gap size are mainly driven by a distribution of metal grain sizes in M1 and M2, with additional factors being the peeling force and direction.<sup>[8, 10]</sup>

Having confirmed a-Lith as a suitable fabrication technique for the development of planar asymmetric electrodes, we identified several conjugated polymers as candidate semiconductors since they combine solution processability and potentially high mobility.<sup>[14-17]</sup> Among those the C<sub>16</sub>IDT-BT polymer (**Figure 2a**) was chosen since it is known to exhibit superior hole transport properties and low contact resistance with Au electrodes in a thin-film transistors (TFTs).<sup>[18-22]</sup> Moreover, recent work has demonstrated that *p*-doping of C<sub>16</sub>IDT-BT can result in improved organic TFTs with reduced contact resistance and record hole mobility<sup>[14, 23-25]</sup>. To explore the potential of doping the organic semiconductor in Schottky diodes, we utilized the molecular *p*-type dopant C<sub>60</sub>F<sub>48</sub> (**Figure 2a**) and studied its impact on the operating characteristics of the planar diodes.

We first assessed the ability of C<sub>60</sub>F<sub>48</sub> to *p*-dope C<sub>16</sub>IDT-BT, since the physical process of charge transfer may be affected by the characteristics of the particular materials involved.<sup>[26]</sup> Calibrated Kelvin Probe (KP) measurements (**Figure 2b**) reveal that the workfunction (WF) in C<sub>16</sub>IDT-BT increases rapidly upon doping with C<sub>60</sub>F<sub>48</sub> from 4.42 eV (pristine polymer, 0 mol%) to 5.11 eV for 5 mol% doping, where it stabilizes. Further details of the measurements procedures can be found in the *Experimental* section. We note that the value of 4.42 eV measured for the pristine C<sub>16</sub>IDT-BT is very close the middle of its bandgap ( $E_G$ ), given as  $|\text{HOMO}| - (E_G/2) = 5.15 - (1.65/2) = 4.32\ \text{eV}$  ( $E_G$  was estimated from the onset of absorption in **Figure 2c**), as would be expected for an intrinsic

semiconductor. On the other hand, the Fermi energy level ( $E_F$ ) undergoes a noticeable shift towards the highest occupied molecular orbital (HOMO) of the polymer (5.15 eV, see inset in **Figure 2b**) upon  $C_{60}F_{48}$  incorporation and plateaus for concentrations >2.5 mol%. This is a characteristic of the  $p$ -doping process and is attributed to the electron transfer from the HOMO of  $C_{16}$ IDT-BT to the lowest unoccupied molecular orbital (LUMO) of  $C_{60}F_{48}$  (inset in **Figure 2b**), in agreement with previous reports.<sup>[23]</sup> The impact of  $p$ -doping on charge transport in  $C_{16}$ IDT-BT was further assessed using field-effect transistor measurements (**Figure S3**). The transfer characteristics of  $C_{16}$ IDT-BT-based transistors with 2.5 mol%  $C_{60}F_{48}$  exhibit a major increase (2-3 orders of magnitude) in the channel off current ( $I_{OFF}$ ) accompanied by a characteristic shift in the threshold voltage ( $V_T$ ) towards zero while the hole mobility remains largely unchanged ( $\sim 0.6 \text{ cm}^2 \text{ V}^{-1} \text{ s}^{-1}$ ). Additional experimental evidence of the  $p$ -doping effect were obtained from ultraviolet-visible (UV-Vis) absorption measurements of  $C_{16}$ IDT-BT films before and after doping with  $C_{60}F_{48}$  at concentrations in the range of 1-5 mol% (**Figure 2c**). From the onset of absorption of the pristine  $C_{16}$ IDT-BT film, the optical  $E_g$  was estimated yielding a value of  $\sim 1.65 \text{ eV}$ . All  $C_{60}F_{48}$ -doped  $C_{16}$ IDT-BT layers exhibit similar onset but with an additional broad polaronic absorption peak centred at  $\sim 1040 \text{ nm}$ , which becomes more intense with increasing dopant concentration (inset, **Figure 2c**), further supporting the  $p$ -dopant character of  $C_{60}F_{48}$ .

Grazing incidence wide angle X-ray scattering (GIWAXS) measurements were also performed to assess the packing motif/microstructure of neat and  $C_{60}F_{48}$ -doped  $C_{16}$ IDT-BT layers (**Figure 2d**). The few diffraction peaks present in the 2D-GIWAXS patterns for the neat  $C_{16}$ IDT-BT and the corresponding in-plane and out-of-plane profiles (**Figure S4**), indicate a low degree of structural order, in agreement with previous reports.<sup>[22]</sup> Addition of  $C_{60}F_{48}$  in the  $C_{16}$ IDT-BT, at different concentrations, does not change the GIWAXS patterns (e.g. appearance of extra peaks or modification of existing ones), meaning that the microstructure of the  $C_{16}$ IDT-BT: $C_{60}F_{48}$  layers remain unaltered. The latter may prove advantageous for application in devices comprised of nanoscale

channels, such as those formed via a-Lith (**Figure 1d**), where structural changes can prove detrimental.

Next, we investigated the potential of the neat and *p*-doped C<sub>16</sub>IDT-BT as the active layer in Schottky diodes based on the asymmetric Au-Al planar electrodes shown in **Figure 1c**. Devices with empty nanogaps (i.e. without semiconductor) show very low current of  $<10^{-10}$  A (**Figure 3a**) confirming the existence of an electrically isolating nanogap. Spin-coating the neat C<sub>16</sub>IDT-BT on top of the Au-Al electrodes, results in devices with highly asymmetric current-voltage (I-V) characteristics with a rectification ratio of  $\geq 10^3$  (**Figure 3a**). Under forward bias (negative potential applied on the Al electrode), holes are injected from the Au electrode and transported across the nanogap channel to recombine at the Al side. Evidently, doping of the C<sub>16</sub>IDT-BT with C<sub>60</sub>F<sub>48</sub> increases the diode's maximum forward current while shifting the  $V_{ON}$  towards 0 V. On the other hand, the diode's reverse current increases with increasing C<sub>60</sub>F<sub>48</sub> concentration, indicating increased carrier recombination at the junction. We attribute this to the presence of C<sub>60</sub>F<sub>48</sub> and its deep LUMO (**Figure 2b**, inset) which could facilitate electron injection from the Au electrode and contribute to the recombination current.<sup>[24]</sup> This hypothesis is supported by the increased dependence of the reverse current on the applied potential (1.5-2 V) seen in **Figure 3a** for 3 mol% C<sub>60</sub>F<sub>48</sub>. A small anti-clock wise hysteresis is present in the I-V curves (**Figure S5**) that appears to become more prominent for higher C<sub>60</sub>F<sub>48</sub> concentrations. This is most likely attributed to C<sub>60</sub>F<sub>48</sub>-induced trap states.<sup>[23]</sup> Importantly, the diode's forward current and rectification ratio can be tailored to a particular application without compromising its dark current by simply adjusting the nanogap width. This is illustrated in **Figure 3b** where scaling of the W in C<sub>16</sub>IDT-BT:C<sub>60</sub>F<sub>48</sub>(2.5 mol%) diodes leads to a tenfold increase of the maximum forward current while maintaining the reverse current low ( $<1$  nA). Although the rectification ratio of our coplanar diodes are on par with previous published data ( $\geq 10^4$ ) on organic diodes<sup>[15]</sup>, the RC constants of our planar nanogap diodes are expected to remain significantly lower.



Next an equivalent-circuit model was developed to describe the planar  $C_{16}$ IDT-BT Schottky diodes using intrinsic and extrinsic components (**Figure S6**). Such models are often used to emulate the actual parameters of Schottky diodes and are extremely useful for the design of more complex integrated circuits such as frequency mixers and voltage pumps.<sup>[27]</sup> In our model the intrinsic part can be broken down into voltage-dependent junction capacitance ( $C_j$ ), junction resistance ( $R_j$ ) and series resistance ( $R_s$ ). Unlike the vertical diode architecture (sandwich type), the planar diode configuration results in fewer extrinsic parasitic components. The air and substrate fringing fields generated across the junction perimeter are modeled as extrinsic parasitic fringing capacitance ( $C_p$ ). The external parasitic capacitance ( $C_{pad}$ ) and inductance ( $L_{pad}$ ) between electrode and ground are negligible due to the good isolation from the external ground and small radial electrode dimensions. The thermionic field emission model that accounts for emission currents, as well as tunnelling of electrons through the barrier, is used to extract the ideality factor ( $n$ ) and the voltage dependent series resistance ( $R_s$ ) for neat and  $C_{60}F_{48}$ -doped (2.5 mol%)  $C_{16}$ IDT-BT devices (**Figure S7**). As summarized in **Table S1**, the voltage dependent  $R_s$  is 2-3 orders of magnitude lower for the  $C_{16}$ IDT-BT: $C_{60}F_{48}$ (2.5 mol%) diode than the pristine one. **Figure S8** shows the simplified advanced design software (ADS) model used for fitting the measured I-V curve while the comparison between measured (symbols) and modeled (lines) data is presented in **Figure 3b**. Overall, the ADS model based on the aforementioned equivalent circuit, was able to reproduce the measured I-V curves and can be seen as a valuable tool for the design of further circuitry.

To gain insights in the role of the  $p$ -dopant, we studied the evolution of the barrier height ( $\Phi_b$ ) in  $C_{16}$ IDT-BT diodes before and after doping with  $C_{60}F_{48}$  (2.5 mol %), using capacitance-voltage (C-V) measurements. The latter is considered to be the most practical method for evaluating the  $\Phi_b$  and the built-in potential ( $V_{bi}$ ) in Schottky diodes.<sup>[12]</sup> **Figure S9a** presents the C-V data for the neat  $C_{16}$ IDT-BT and  $p$ -doped  $C_{16}$ IDT-BT: $C_{60}F_{48}$ (2.5 mol%) diodes obtained at 1, 10, and 100 kHz. To improve the accuracy of our calculations, the extrinsic capacitances attributed to the 3D coupling of the

planar nanogap electrode architecture and the glass substrate, were estimated and appropriate corrections to the measured capacitance were applied using previously established protocols.<sup>[12]</sup> The corrected Mott-Schottky plots obtained at 1 kHz for the C<sub>16</sub>IDT-BT and C<sub>16</sub>IDT-BT:C<sub>60</sub>F<sub>48</sub>(2.5 mol%) diodes are shown in **Figure S9b**. As expected, the  $\Phi_b$  and  $V_{bi}$  for the C<sub>16</sub>IDT-BT:C<sub>60</sub>F<sub>48</sub>(2.5 mol%) diodes are significantly lower (0.6 eV and -0.4 V) than C<sub>16</sub>IDT-BT diodes (1.6 eV and -1.4 V). The plateau observed in the near zero voltage region is attributed to shallow trap states induced by the molecular dopant.<sup>[23, 24]</sup> To better understand the contribution of each component on the diode operation, the total capacitance was modelled using

$$C_{total} = C_j + C_p = \frac{C_{j0}}{\sqrt{1 - \frac{V}{\Phi_{bi}}}} + C_p \quad (2)$$

where  $\Phi_{bi}$  is built-in potential,  $C_{j0}$  is zero bias junction capacitance and  $C_p$  accounts for parasitic capacitance due to the fringing fields present between the electrodes. The linear part of the experimentally determined  $1/C^2$  vs.  $V$  curve (Mott-Schottky plot) was then used as the curve-fitting region. We employed the Levenberg-Manquardt algorithm to fit Eq. 2 to the measured C-V data in order to extract  $C_{j0}$  and  $C_p$  values (**Figure S9c**) yielding  $4.8 \times 10^{-13}$  and  $1.4 \times 10^{-14}$  F, respectively, for neat C<sub>16</sub>IDT-BT, and  $\sim 9 \times 10^{-13}$  and  $\sim 2.2 \times 10^{-14}$  F, respectively, for *p*-doped C<sub>16</sub>IDT-BT:C<sub>60</sub>F<sub>48</sub>(2.5 mol%) diodes. The slightly increase  $C_{j0}$  in the latter is attributed to the narrowing of the depletion region width<sup>[28]</sup>, and/or the increase of the accumulation region over larger parts of the electrodes near the nanogap region.

Next we looked into the high frequency characteristics of our planar organic Schottky diodes. We note that as of to date there is only a handful of reports on organic Schottky diodes operating in the GHz frequency range. To the best of our knowledge, the work by Kang *et al.* on pentacene Schottky diodes operating at  $\sim 1$  GHz represents the best performance reported to-date.<sup>[29]</sup> To evaluate the frequency response of our C<sub>16</sub>IDT-BT planar diodes, one-port scattering parameter

( $S_{11}$ ) measurements were used to extract the impedance and the intrinsic cut-off frequency ( $f_{C-Int.}$ ) of the devices.<sup>[30-32]</sup> The  $f_{C-Int.}$  can be estimated from the intersection point of the real (Real  $R_s$ ) and imaginary (Imag  $X_b$ ) parts of the impedance curves shown in **Figure 4a**. Evidently, both pristine  $C_{16}$ IDT-BT and  $p$ -doped  $C_{16}$ IDT-BT: $C_{60}F_{48}$ (2.5 mol%) diodes with  $W = 5000 \mu m$  exhibit intrinsic cut-off frequencies well above 1 GHz, clearly highlighting the advantage of the asymmetric nanogap architecture. The  $f_{C-Int.}$  for the doped  $C_{16}$ IDT-BT: $C_{60}F_{48}$ (2.5 mol%) diodes is slightly higher ( $\sim 8$  GHz) than for undoped  $C_{16}$ IDT-BT diodes ( $\sim 6$  GHz), with both types of devices exhibiting a strong dependence on nanogap width, where a clear uptrend in  $f_{C-Int.}$  with reducing  $W$  (**Figure S10**), due to reduced  $C_j$  (**Figure S11**), is observed. Importantly, the planar nanogap diodes are characterized by low capacitances of  $< 2$  pF up to 10 GHz, making them ideal for high frequency applications.

In order to explore the full potential of the technology, the extrinsic cut-off frequency ( $f_{C-Ext.}$ ) of our planar diodes was determined experimentally using a rectifier circuit comprised of a tee bias and load resistor (**Figure 4b**) in the frequency range of 0.1 GHz to 18 GHz. For simplicity, no matching circuit was used and as a result the actual power delivered to the diode is expected to be considerably lower than the nominal power outputted by the vector network analyzer (VNA) due to impedance mismatch. The  $f_{C-Ext.}$  was extracted from the half-power point where the rectified DC voltage ( $V_{OUT}$ ) drops to 0.707 of its initial maximum value.<sup>[10, 33]</sup> Though there is only a small difference in the extracted  $f_{C-Ext.}$  between pristine  $C_{16}$ IDT-BT and  $p$ -doped  $C_{16}$ IDT-BT: $C_{60}F_{48}$ (2.5 mol%) diodes, the  $V_{OUT}$  increases by tenfold upon doping (**Figure 4c**). This major improvement is the result of favorable synergistic effects induced by the dopant and include; (i) a reduced  $\Phi_b$ , (ii) a lower  $V_{bi}$ , and (iii) a dramatically suppressed  $R_s$  ( $10^7$ - $10^{10} \Omega$  for pristine vs.  $10^5$ - $10^7 \Omega$  for  $p$ -doped devices, **Table S1**). Interestingly, the DC  $V_{OUT}$  is found to scale with the diode's  $W$  (**Figure 4d-e** and **Figure S11**) as well as with the nominal power of the input signal (**Figure S13**). We attribute this to the improved impedance matching upon doping, which also highlights the possibility for further improvements. Increasing  $P_{in}$  to 17 dBm leads to diode breakdown followed by a sudden drop in  $V_{OUT}$ . The latter

highlights the limitations on the power handling capabilities of these devices which is a consequence of their breakdown characteristics (**Figure S14**). Despite this, however, the diodes should be well suited for low power applications such as energy harvesting circuits for IoT, and emerging telecommunication systems.<sup>[34]</sup>

The  $f_{C-Ext.}$  for both  $C_{16}$ IDT-BT and  $p$ -doped  $C_{16}$ IDT-BT: $C_{60}F_{48}$ (2.5 mol%) diodes increases with reducing  $W$ , due to lower capacitance, reaching an unprecedented maximum value of  $\sim 14$  GHz for the 250  $\mu m$ -width  $p$ -doped diode (**Figure 4f**). The I-V and RF performance of several devices manufactured on the same chip are also shown in **Figure S15** and highlight the potential of a-Lith for reliable manufacturing of organic RF electronics over large area substrates. However, one noticeable drawback is the sensitivity of the electrical performance of these coplanar diodes towards ambient atmosphere over time (**Figure S16**). To this end, we anticipate significant improvements to be possible via encapsulation, and/or through the use of alternative organic semiconductors. For example, use of highly crystalline small molecule semiconductors that combine high carrier mobility with ambient stability could lead to significant performance boost. Despite this issue the level of performance of our organic Schottky diodes surpasses all previously published data, clearly highlighting the tremendous advantage of the planar nanogap architecture. This is better illustrated in **Figure 4g** where the  $f_{C-Ext.}$  of best-performing organic Schottky diodes reported to date are summarized. In this plot one can clearly see the large upward jump in performance enabled by our planar nanogap  $C_{16}$ IDT-BT diodes, placing them well within the 5G frequency spectrum for the first time.

In summary, we have shown that combining asymmetric self-aligned nanogap electrodes patterned by a-Lith with the high mobility organic polymer  $C_{16}$ IDT-BT, enables the development of the first organic Schottky diodes operating within the 5G frequency spectrum. Molecular doping of the polymer semiconductor was used to enhance the performance of the diodes highlighting the

potential for further improvements. For example, use of suitable self-assembled monolayers (SAMs) as electrode work function modifiers could be explored to lower the contact resistance further and increase both the  $f_{C-Ext}$  and  $V_{OUT}$ . Similar improvements could be anticipated through the use of organic semiconductors with higher mobility<sup>[40]</sup>, and/or improved doping schemes<sup>[41]</sup>. Overall, our approach described in this study addresses inherent limitations associated with conventional organic Schottky diodes and paves the way to further research towards cost-effective RF electronics. We expect that the simplicity, large-area compatibility, and possibility for monolithic integration of our organic diodes with antennas and other passive and active components, makes them an attractive technology for application in wireless energy harvesting and telecommunications in the forthcoming IoT era.

## Experimental

*Adhesion lithography for nanogap electrode fabrication:* Thermally evaporated Aluminium (Al) films were patterned on Borofloat glass substrates using conventional photolithography via bright field patterning and wet chemical etching. The patterned substrates were immersed in 1 mM (7.8 mg of octadecylphosphonic acid in 30 mL of isopropyl alcohol) solution for 20 hours to allow the formation of self-assembled monolayer (SAM) on Al (M1 electrode). The substrates were rinsed with isopropyl alcohol to ensure the removal of physisorbed SAM on the substrates then dried at 80 °C in air on a hotplate for 15 minutes. Next, a 5/95 nm thick Al/Au films (M2 electrode) was evaporated on top of the entire substrate. The 5 nm of Al was used to promote the adhesion between the Au electrode and the substrate. Due to the reduced adhesion between M2 and M1/SAM, the selective removal of M2 was achieved by applying a glue (First Contact) to the surface of the sample followed by a mechanical peel-off step. The selective removal of the overlapping M2 causes the formation of a nanogap between M1 and M2. The SAM atop M1 was then removed by 2 min of Ar plasma treatment prior to the semiconductor layer deposition.

This article is protected by copyright. All rights reserved.

*Material Preparation:* C<sub>16</sub>IDT-BT ( $M_n$  65 kg mol<sup>-1</sup> with a dispersity ( $\bar{D}$ ) of 2.42 as measured by GPC in chlorobenzene at 80 °C against polystyrene standards) and C<sub>60</sub>F<sub>48</sub> were synthesized using previously reported procedures.<sup>[35, 36]</sup> Anhydrous chlorobenzene (CB) and 1,2- dichlorobenzene (oDCB) was purchased from Sigma-Aldrich and used as received. Solutions of C<sub>16</sub>IDT-BT (5 mg/ml in oDCB) were prepared and stirred overnight at 100°C, while solutions of C<sub>60</sub>F<sub>48</sub> (1 mg/ml in CB) were stirred overnight at room temperature. The dopant solution was then added to the semiconductor solution in order to obtain the required concentration, which was calculated in mol% of the dopant in respect to the molecular weight of one monomer of the polymer. Doped solutions were then stirred for 2 hours at room temperature and spin-coated at 1000 rpm for 60 seconds, followed by an annealing treatment of 2 minutes to remove the excess of solvent. The entire process was carried out in a nitrogen-filled glovebox.

*Scanning Electron Microscope (SEM):* The SEM topology images of Al/Al-Au nanogap electrodes were acquired by an ultra-high resolution field emission Magellan SEM equipped with 2-mode final lens (immersion and field-free). The high resolution images were obtained using the immersion mode at 5-10 kV after appropriate beam and lens alignments.

*UV-Vis absorption spectroscopy:* Absorption spectra were measured with a Shimadzu UV-2600 spectrophotometer.

*Kelvin-probe work-function measurement:* Work function measurements of pristine and p-doped C<sub>16</sub>IDT-BT films were carried out using the Kelvin Probe technique using a KP Technology SPS040 system. Samples were prepared by depositing polymer films with doping concentrations between 0-5 mol% on top of ITO covered glass slides. As reference material we used a freshly cleaned highly oriented pyrolytic graphite (HOPG) film with an expected work function of ~4.5 eV. Since this reference value for HOPG was not measured directly, the actual values given in **Figure 2b** might be subject to small, but systematic, deviation. As such we expect that the progression of work function changes due to increased dopant concentration to remain the same, regardless of the absolute value of

the reference HOPG. To minimize unwanted effects (e.g. adsorption of water and oxygen) all measurements were carried out inside a dry nitrogen filled glove box.

*Grazing Incidence Wide Angle X-Ray Scattering (GIWAXS):* Diffraction patterns at grazing incidence were taken at the BL11, NCD-SWEET, beamline at ALBA Synchrotron, Cerdanyola del Vallès (Spain). The energy beam was set at 12.4 keV ( $\lambda = 0.1$  nm) using a channel cut Si (1 1 1) monochromator. The incident angle was set at  $0.12^\circ$  and the exposition time was 5 sec. GIWAXS patterns were taken with a Rayonix® LX255-HS area detector (pixel size of 88 microns), placed at 210 mm from the sample position. 2D-GIWAXS patterns were corrected as a function of the components of the scattering vector with a Matlab® script developed by Aurora Nogales and Edgar Gutiérrez [<https://it.mathworks.com/matlabcentral/fileexchange/71958-grazing-incidence-wide-angle-x-ray-scattering-representation>]. Material solutions were prepared and processed following the same procedures used for the device fabrication on top of silicon substrates.

*Organic transistors fabrication and characterization:* OTFTs were fabricated with a top-gate, bottom-contact (TG-BC) architecture onto  $2.54 \times 2.54$  cm<sup>2</sup> glass substrates. The source/drain electrodes composed of Al/Au (5/35 nm) were defined with shadow masks via thermal evaporation. The substrates were then cleaned by sonication in acetone and isopropanol, followed by an Argon plasma treatment for 2 min. Pristine and C<sub>60</sub>F<sub>48</sub>-doped C<sub>16</sub>IDT-BT solutions were prepared and spin-coated on top of the substrates following the same procedures employed for the nanogap diodes fabrication (i.e. 1000 rpm for 60 s at RT), followed by an annealing step at 100 °C for 2 min. Cytop, acting as the gate dielectric, was then spin-coated atop the organic layer at 4000 rpm for 90 s (thickness ~600 nm) and annealed at 80 °C for 1 h. The Al gate electrode was then thermally evaporated through a shadow mask. Finally, the devices were transferred to the measurement setup inside a nitrogen-filled glovebox using a transfer tube. Electrical characterization was performed with an Agilent B2902A semiconductor parameter analyser.

*Diode characterization:* The current–voltage (I-V) characteristics of the diodes were measured using Keysight B2912A precision source-meter. The capacitance measurements were performed using a Keysight B1500A semiconductor device analyser. All electrical measurements were carried out inside a nitrogen-filled glovebox.

*Radio frequency measurements:* The one-port scattering parameter ( $S_{11}$ ) measurements in the frequency range 0.01-50 GHz were measured in ambient conditions using an Agilent Network analyser (PNA N5225A) connected to a Cascade Microtech probe station. Cascade Infinity GSG probes (ACP-40) having a pitch of 250  $\mu\text{m}$  were used with the valid Open, Short and Load (OSL) calibration on impedance standard substrate (ISS) of 106-682. The rectifier circuit measurements were carried out inside the nitrogen-filled glovebox using tee bias (0.1 MHz-18 GHz, from Pasternack), a 10 M $\Omega$  load resistor and a Keysight 34465A digital multi-meter.

### Supporting Information

Supporting Information is available from the Wiley Online Library or from the author.

### Acknowledgments

This publication is based upon work supported by the King Abdullah University of Science and Technology (KAUST), KAUST Solar Centre Office of Sponsored Research (OSR) under Award No: OSR-2018-CARF/CCF-3079 and Award No: OSR-2020-CRG9-4347.

Received: ((will be filled in by the editorial staff))

Revised: ((will be filled in by the editorial staff))

Published online: ((will be filled in by the editorial staff))



## References

- [1] J. Semple, D. G. Georgiadou, G. Wyatt-Moon, G. Gelinck, T. D. Anthopoulos, *Semicond. Sci. Technol.* **2017**, 32, 123002.
- [2] S. Dang, O. Amin, B. Shihada, M.-S. Alouini, *Nat. Electronics* **2020**, 3, 20.
- [3] S. Kim, R. Vyas, J. Bito, K. Niotaki, A. Collado, A. Georgiadis, M. M. Tentzeris, *Proceedings of the IEEE* **2014**, 102, 1649.
- [4] M. Cansiz, D. Altinel, G. K. Kurt, *Energy* **2019**, 174, 292.
- [5] C. R. Valenta, G. D. Durgin, *IEEE Microw. Mag.* **2014**, 15, 108.
- [6] Y. Chu, C. Qian, P. Chahal, C. Cao, *Adv. Sci.* **2019**, 6, 1801653.
- [7] U. Zschieschang, J. W. Borchert, M. Giorgio, M. Caironi, F. Letzkus, J. N. Burghartz, U. Waizmann, J. Weis, S. Ludwigs, H. Klauk, *Adv. Funct. Mater.* **2019**, 30, 1903812.
- [8] D. J. Beesley, J. Semple, L. Krishnan Jagadamma, A. Amassian, M. A. McLachlan, T. D. Anthopoulos, J. C. deMello, *Nat. Commun.* **2014**, 5, 3933.
- [9] W.-Y. Uhm, S.-G. Choi, M. Han, K.-K. Ryu, S.-C. Kim, *J. Elect. Engg. and Tech.* **2016**, 11, 1367.
- [10] D. G. Georgiadou, J. Semple, A. A. Sagade, H. Forstén, P. Rantakari, Y.-H. Lin, F. Alkhalil, A. Seitkhan, K. Loganathan, H. Faber, T. D. Anthopoulos, *Nat. Electronics* **2020**, 3, 718.
- [11] J. Semple, S. Rossbauer, C. H. Burgess, K. Zhao, L. K. Jagadamma, A. Amassian, M. A. McLachlan, T. D. Anthopoulos, *Small* **2016**, 12, 1993.
- [12] J. Semple, S. Rossbauer, T. D. Anthopoulos, *ACS Appl. Mater. Interfaces* **2016**, 8, 23167.
- [13] S. Kano, T. Kawazu, A. Yamazaki, M. Fujii, *Nanotechnology* **2019**, 30, 285303.
- [14] A. Basu, M. R. Niazi, A. D. Scaccabarozzi, H. Faber, Z. Fei, D. H. Anjum, A. F. Paterson, O. Boltalina, M. Heeney, T. D. Anthopoulos, *J. Mater. Chem. C* **2020**, 8, 15368.
- [15] M. Cao, W. J. Hyun, L. F. Francis, C. D. Frisbie, *Flex. Print. Electron.* **2020**, 5, 015006.
- [16] A. M. Zeidell, D. S. Filston, M. Waldrip, H. F. Iqbal, H. Chen, I. McCulloch, O. D. Jurchescu, *Adv. Mater. Technol.* **2020**, 5, 2000390.
- [17] J. Yang, Z. Zhao, S. Wang, Y. Guo, Y. Liu, *Chem* **2018**, 4, 2748.
- [18] M. Nikolka, I. Nasrallah, B. Rose, M. K. Ravva, K. Broch, A. Sadhanala, D. Harkin, J. Charmet, M. Hurhangee, A. Brown, S. Illig, P. Too, J. Jongman, I. McCulloch, J. L. Bredas, H. Sirringhaus, *Nat. Mater.* **2017**, 16, 356.

This article is protected by copyright. All rights reserved.

- [19] Z. A. Lamport, K. J. Barth, H. Lee, E. Gann, S. Engmann, H. Chen, M. Guthold, I. McCulloch, J. E. Anthony, L. J. Richter, D. M. DeLongchamp, O. D. Jurchescu, *Nat. Commun.* **2018**, 9, 5130.
- [20] D. Venkateshvaran, M. Nikolka, A. Sadhanala, V. Lemaire, M. Zelazny, M. Kepa, M. Hurhangee, A. J. Kronemeijer, V. Pecunia, I. Nasrallah, I. Romanov, K. Broch, I. McCulloch, D. Emin, Y. Olivier, J. Cornil, D. Beljonne, H. Sirringhaus, *Nature* **2014**, 515, 384.
- [21] A. Wadsworth, H. Chen, K. J. Thorley, C. Cendra, M. Nikolka, H. Bristow, M. Moser, A. Salleo, T. D. Anthopoulos, H. Sirringhaus, I. McCulloch, *J Am Chem Soc* **2020**, 142, 652.
- [22] X. Zhang, H. Bronstein, A. J. Kronemeijer, J. Smith, Y. Kim, R. J. Kline, L. J. Richter, T. D. Anthopoulos, H. Sirringhaus, K. Song, M. Heeney, W. Zhang, I. McCulloch, D. M. DeLongchamp, *Nat. Commun.* **2013**, 4, 2238.
- [23] A. F. Paterson, N. D. Treat, W. Zhang, Z. Fei, G. Wyatt-Moon, H. Faber, G. Vourlias, P. A. Patsalas, O. Solomeshch, N. Tessler, M. Heeney, T. D. Anthopoulos, *Adv Mater* **2016**, 28, 7791.
- [24] A. F. Paterson, Y.-H. Lin, A. D. Mottram, Z. Fei, M. R. Niazi, A. R. Kirmani, A. Amassian, O. Solomeshch, N. Tessler, M. Heeney, T. D. Anthopoulos, *Adv. Electron. Mater.* **2018**, 4, 1700464.
- [25] A. D. Scaccabarozzi, F. Scuratti, A. J. Barker, A. Basu, A. F. Paterson, Z. Fei, O. Solomeshch, A. Petrozza, N. Tessler, M. Heeney, T. D. Anthopoulos, M. Caironi, *Adv. Electron. Mater.* **2020**, 6, 2000539.
- [26] I. E. Jacobs, A. J. Moule, *Adv Mater* **2017**, 29, 1703063.
- [27] A. Y. Tang, V. Drakinskiy, K. Yhland, J. Stenarson, T. Bryllert, J. Stake, *IEEE Trans. Microw. Theory Tech.* **2013**, 61, 1870.
- [28] S. M. N. Sze, Kwok K., *Physics of Semiconductor Devices*, John Wiley & Sons, Inc., 2007.
- [29] C.-m. Kang, J. Wade, S. Yun, J. Lim, H. Cho, J. Roh, H. Lee, S. Nam, D. D. C. Bradley, J.-S. Kim, C. Lee, *Adv. Electron. Mater.* **2016**, 2, 1500282.
- [30] J. Zhang, Y. Li, B. Zhang, H. Wang, Q. Xin, A. Song, *Nat. Commun.* **2015**, 6, 7561.
- [31] J. Zhang, H. Wang, J. Wilson, X. Ma, J. Jin, A. Song, *IEEE Electron Device Lett.* **2016**, 37, 389.
- [32] S. J. Yang, K. T. Park, J. Im, S. Hong, Y. Lee, B. W. Min, K. Kim, S. Im, *Nat. Commun.* **2020**, 11, 1574.
- [33] X. Zhang, J. Grajal, J. L. Vazquez-Roy, U. Radhakrishna, X. Wang, W. Chern, L. Zhou, Y. Lin, P. C. Shen, X. Ji, X. Ling, A. Zubair, Y. Zhang, H. Wang, M. Dubey, J. Kong, M. Dresselhaus, T. Palacios, *Nature* **2019**, 566, 368.
- [34] X. Zhang, J. Grajal, M. López-Vallejo, E. McVay, T. Palacios, *Joule* **2020**, 4, 1148.
- [35] W. Zhang, J. Smith, S. E. Watkins, R. Gysel, M. McGehee, A. Salleo, J. Kirkpatrick, S. Ashraf, T. Anthopoulos, M. Heeney, I. McCulloch, *J. Am. Chem. Soc.* **2010**, 132, 11437.

- [36] A. V. Kepman, V. F. Sukhoverkhov, A. Tressaud, C. Labrugere, E. Durand, N. S. Chilingarov, L. N. Sidorov, *J. Fluor. Chem.* **2006**, 127, 832.
- [37] Y. Smets, C. B. Stark, F. Schmitt, M. T. Edmonds, S. Lach, C. A. Wright, D. P. Langley, K. J. Rietwyk, A. Schenk, A. Tadich, M. Wanke, C. Ziegler, L. Ley, C. I. Pakes, *Org. Electron.* **2013**, 14, 169.
- [38] M. T. Edmonds, M. Wanke, A. Tadich, H. M. Vulling, K. J. Rietwyk, P. L. Sharp, C. B. Stark, Y. Smets, A. Schenk, Q. H. Wu, L. Ley, C. I. Pakes, *J. Chem. Phys.* **2012**, 136, 124701.
- [39] K. J. Rietwyk, M. Wanke, H. M. Vulling, M. T. Edmonds, P. L. Sharp, Y. Smets, Q. H. Wu, A. Tadich, S. Rubanov, P. J. Moriarty, L. Ley, C. I. Pakes, *Phy. Rev. B* **2011**, 84, 035404.
- [40] A. F. Paterson, S. Singh, K. J. Fallon, T. Hodsden, Y. Han, B. C. Schroeder, H. Bronstein, M. Heeney, I. McCulloch, T. D. Anthopoulos, *Advanced Materials* **2018**, 30, 1801079.
- [41] A. D. Scaccabarozzi, A. Basu, F. Aniés, J. Liu, O. Zapata-Arteaga, R. Warren, Y. Firdaus, M. I. Nugraha, Y. Lin, M. Campoy-Quiles, N. Koch, C. Müller, L. Tsetseris, M. Heeney, T. D. Anthopoulos, *Chemical Reviews* **2021**, ASAP article, <https://doi.org/10.1021/acs.chemrev.1c00581>

## Figures

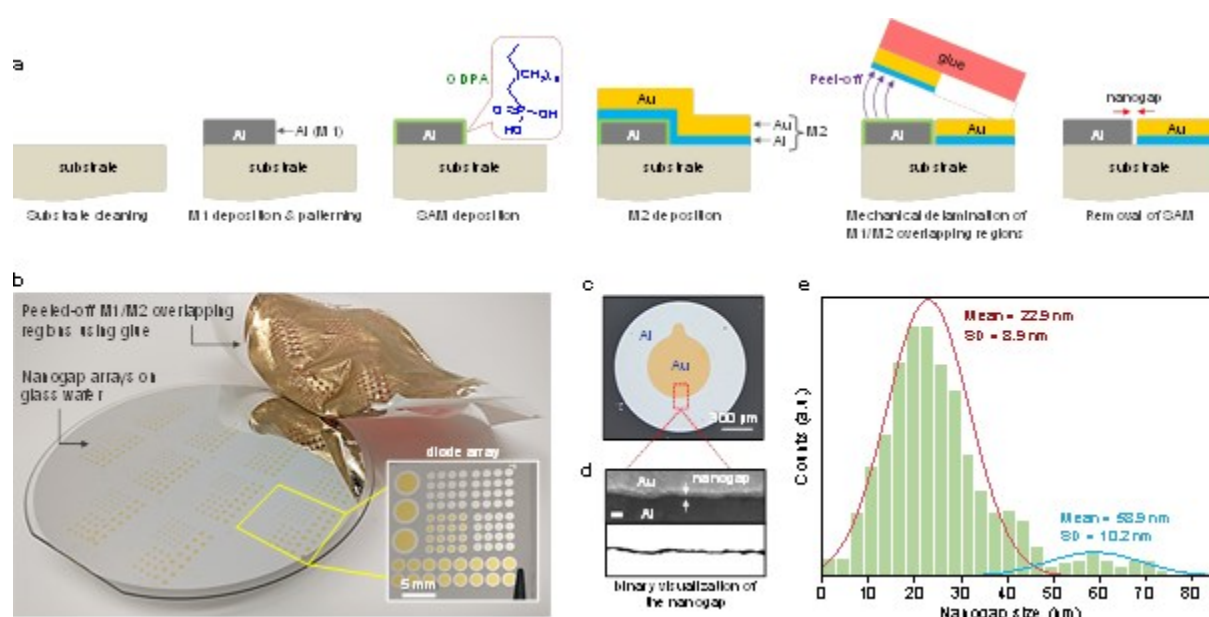


**Figure 1.** (a) Schematic illustrations of the adhesion lithography (a-Lith) process steps. (b) A photograph showing the peel-off step and removal of the overlapping regions of the bimetallic M2 electrode (Al-Au) from the surface of M1-SAM electrode across a 4 inch glass wafer. The inset photograph shows a diced chip containing an array of circular, self-aligned planar Al/Al-Au nanogap electrodes. (c) A high resolution optical microscope image of a single nanogap device. (d) SEM image of the nanogap formed between M1 and M2 and the corresponding binary visualization where only the area within the gap is shown as dark pixels. The scale bar is 100 nm. (e) Histogram summarizing the combined nanogap size distribution obtained from five Al/Al-Au SEM images (see **Figure S2**). The gap size extraction followed a method adapted from Kano et al.<sup>[13]</sup>

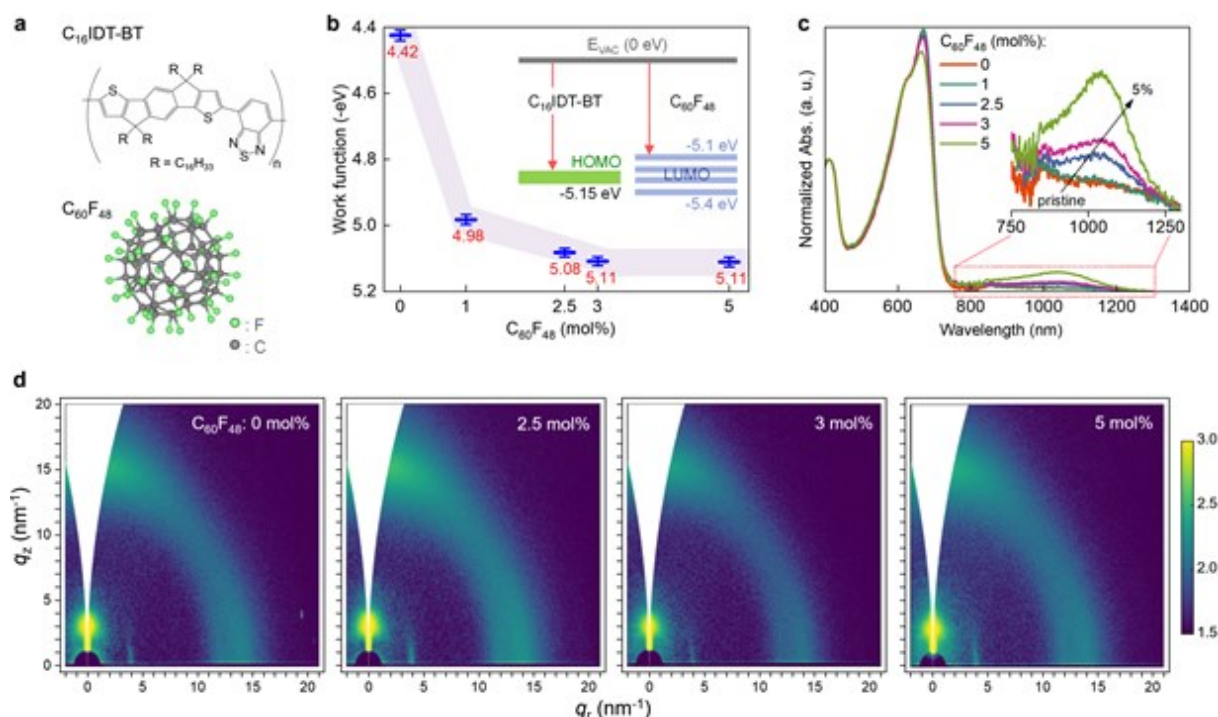


**Figure 2.** (a) Chemical structures of the  $C_{16}$ IDT-BT polymer and the molecular  $p$ -dopant  $C_{60}F_{48}$ . (b) Evolution of the work function (WF) of  $C_{16}$ IDT-BT with dopant concentration measured via Kelvin Probe. For each sample tested the WF was calculated using a cleaned highly oriented pyrolytic graphite (HOPG) sample with a WF of 4.5 eV as the reference electrode. All measurements were performed inside a nitrogen-filled glovebox. The inset presents (not in scale) the HOMO and LUMO energy levels for  $C_{16}$ IDT-BT<sup>[23]</sup> and  $C_{60}F_{48}$ <sup>[37-39]</sup>, respectively. (c) Absorption spectra for neat and  $C_{60}F_{48}$ -doped  $C_{16}$ IDT-BT polymer films. The inset shows the polaron peaks at 1040 nm. (d) Grazing incidence wide angle X-ray scattering (GIWAXS) patterns for neat and  $C_{60}F_{48}$ -doped  $C_{16}$ IDT-BT polymer layers.

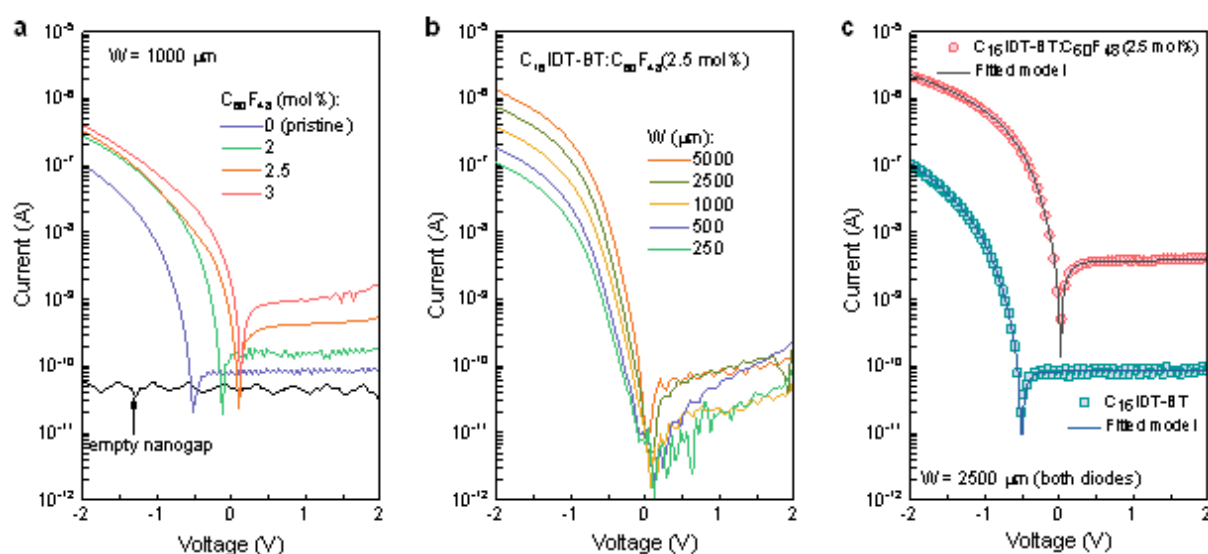


**Figure 3.** (a) Current-voltage (I-V) characteristics of Al-Au nanogap diodes based on pristine  $C_{16}IDT-BT$  and  $C_{60}F_{48}$ -doped  $C_{16}IDT-BT$  with different concentrations in the range 0-3 mol%. (b) I-V characteristics of  $p$ -doped  $C_{16}IDT-BT:C_{60}F_{48}(2.5 \text{ mol}\%)$  diodes with different channel widths ( $W$ ) in the range 250-5000  $\mu m$ . (c) Experimental I-V curves (symbols) measured from pristine  $C_{16}IDT-BT$  and  $C_{16}IDT-BT:C_{60}F_{48}(2.5 \text{ mol}\%)$  diodes fitted with the ADS model (solid lines). Both diodes in (c) had the same width ( $W$ ) of 2500  $\mu m$ .

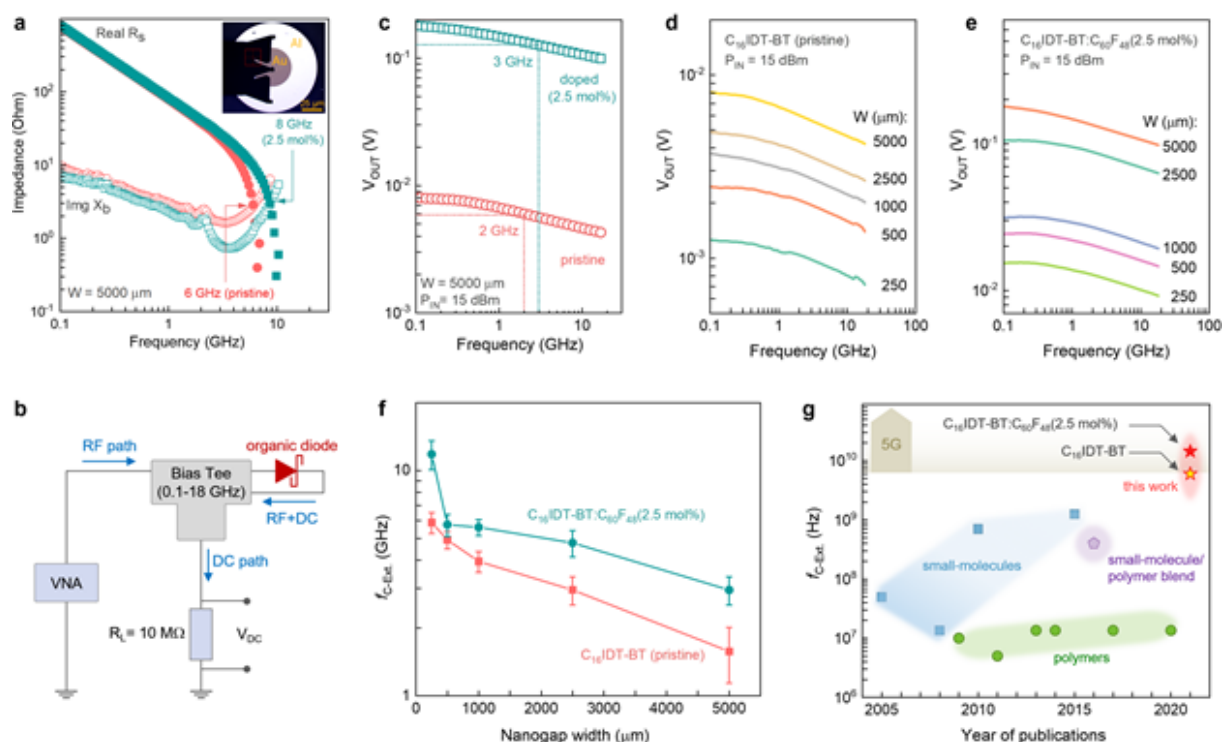


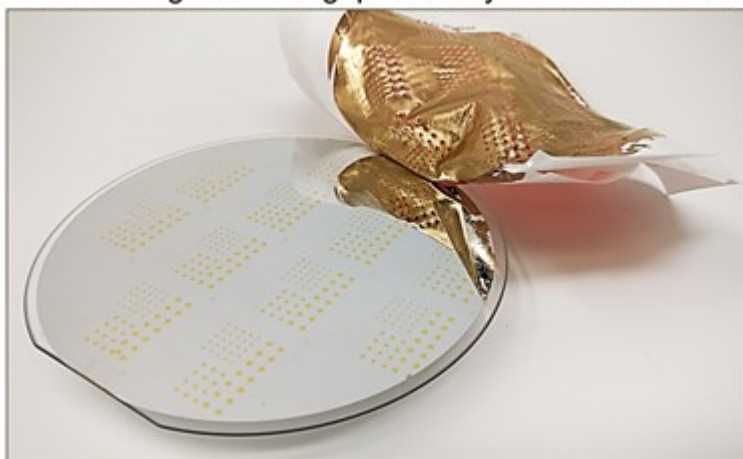
**Figure 4.** (a) Frequency dependent impedance of neat C<sub>16</sub>IDT-BT and C<sub>16</sub>IDT-BT:C<sub>60</sub>F<sub>48</sub>(2.5 mol%) polymer diodes with W= 5000 μm. (b) Circuit diagram of the high frequency rectifier measurement setup used. (c) High frequency rectified voltage output (V<sub>DC</sub>) for neat and *p*-doped (2.5 mol%) C<sub>16</sub>IDT-BT polymer diodes with W = 5000 μm. (d-e) Dependence of V<sub>OUT</sub> on input signal frequency for neat C<sub>16</sub>IDT-BT and C<sub>16</sub>IDT-BT:C<sub>60</sub>F<sub>48</sub>(2.5 mol%) diodes of varying width (250, 500, 1000, 2500, and 5000 μm). (f) Evolution of the calculated extrinsic cut-off frequency (f<sub>C-Ext.</sub>) for neat C<sub>16</sub>IDT-BT and C<sub>16</sub>IDT-BT:C<sub>60</sub>F<sub>48</sub>(2.5 mol%) diodes with the diodes width in the range 250-5000 μm. (g) Reported f<sub>C-Ext.</sub> for various organic diodes over the past 20 years including this work.



## 14 GHz Schottky Diodes using a *p*-Doped Organic Polymer

*Kalaivanan Loganathan, Alberto D. Scaccabarozi, Hendrik Faber, Federico Ferrari, Zhanibek Bizak, Emre Yengel, Dipti R. Naphade, Murali Gedda, Qiao He, Olga Solomeshch, Begimai Adilbekova, Emre Yarali, Leonidas Tsetseris, Khaled N. Salama, Martin Heeney, Nir Tessler, and Thomas D. Anthopoulos*

14 GHz Organic Nanogap Schottky Diodes via a-Lith



### ToC text

Combining asymmetric co-planar nanogap electrodes with a *p*-doped organic polymer semiconductor yields Schottky diodes that are capable of operating at 14 GHz making them the fastest organic electronic devices reported to date.